

A Novel Camera-to-Robot Calibration Method for Vision-Based Floor Measurements

Jan Andre Rudolph, Dennis Haitz, Markus Ulrich

Machine Vision Metrology Lab, Institute of Photogrammetry and Remote Sensing, Karlsruhe Institute of Technology, Germany
jan.rudolph@kit.edu, dennis.haitz@kit.edu, markus.ulrich@kit.edu

Keywords: Robot Positioning, Robot-Camera-Calibration, Autonomous Guided Vehicle, Machine Vision, Industrial Surveying

Abstract

A novel hand-eye calibration method for ground-observing mobile robots is proposed. While cameras on mobile robots are common, they are rarely used for ground-observing measurement tasks. Laser trackers are increasingly used in robotics for precise localization. A referencing plate is designed to combine the two measurement modalities of laser-tracker 3D metrology and camera-based 2D imaging. It incorporates reflector nests for pose acquisition using a laser tracker and a camera calibration target that is observed by the robot-mounted camera. The procedure comprises estimating the plate pose, the plate-camera pose, and the robot pose, followed by computing the robot-camera transformation. Experiments indicate sub-millimeter repeatability.

1. Introduction

Robot systems have been utilized in industrial facilities for decades to automatize production. This can be traced back to the so-called *second industrial revolution*, which included the use of conveyor belts, as famously implemented by companies such as the Ford Motor Company. However, such automation strategies were targeted at the transport of products within the manufacturing process. For specialized manufacturing tasks, in the 1960s and onwards (Zamalloa et al., 2017; Gasparetto and Scalera, 2019) robot arms began to emerge as a new automation strategy. Robot arms could be utilized for not only short-range transportation but also welding or soldering, or more generally, product assembly. Automatic quality inspection through mounted optical devices is another important industry-relevant task. Other types of robot systems with fewer degrees of freedom are used for tasks like pick-and-place, sorting or machine loading (Gasparetto and Scalera, 2019). In recent years, a different type of robot system has been introduced in industrial manufacturing in the form of mobile platforms. Although mobile platforms also include unmanned aerial vehicles (UAVs), in manufacturing environments and especially logistics, ground-based systems are increasingly used for transportation tasks (Perez-Grau et al., 2021; Tehrani et al., 2022). Those ground-based mobile platforms can be categorized into path-dependent, e.g. by following markers on the ground detected through optical sensing, and fully autonomous systems. Often, the positioning of such systems is implemented using inertial measurement units (IMU) or with optical sensors like cameras or LiDAR. Both optical sensors and IMUs can also be used within an integrated setup for computing the position, orientation, and environment map within a Simultaneous Localization and Mapping (SLAM) algorithm, or visual SLAM, if optical sensors are available.

While ready-to-use mobile platforms often include positioning systems and ground-facing cameras, these are usually used for path detection. There are tasks, however, which require high precision positioning of a mobile system w.r.t. ground-based markers. The mobile robot Rita has been developed for sub-millimeter precise positioning w.r.t. known marker positions on the ground of large production and logistics facilities (Naab et al., 2025). Marking and detecting those markings for high precision ground drillings is its core development objective. A

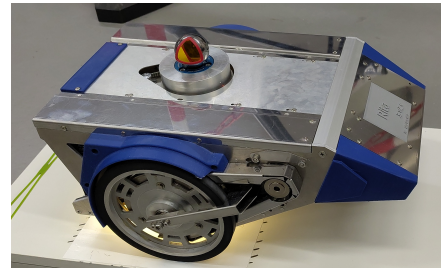


Figure 1. Mobile robot Rita (adapted from Naab (2023)), used in the proposed experiments. It features a differential drive with a front-mounted castor wheel. A spherically mounted retro-reflector is installed on top within a rotatable mount, maintaining the line of sight to a laser tracker. The nadir-mounted camera remains occluded in this image, with only its active illumination apparent.

stationary laser tracker as a polar measurement system is used to accurately determine the position of a platform-mounted reflector with a distance measurement precision of $10 \mu\text{m/m}$. To detect the marking on the ground, a ground-facing, calibrated RGB camera with industrial specifications is built into the mobile platform. Acquired images of the ground below the platform are then utilized to determine the coordinates of a marking in image space. The objective of this research is to transform these image coordinates from the camera coordinate system (CCS) to the robot coordinate system (RCS), which requires a relative orientation between both systems. Over the course of development, we discovered that proven methods for camera-to-robot calibration were not applicable for our case, resulting in insufficient accuracy. Therefore, in this work, we present a specialized calibration procedure. We introduce a standard circular grid calibration plate, which is customized with three colored (red, green, and blue) circles and a reflector within each of the three circles. The mobile platform moves upon the ground laying plate to a first position and acquires an image of the plate, whereby the laser tracker measures the position of the platform by using the reflectors. Then, the mobile platform is moved to a second position and the laser tracker measures the new position of the platform, as well as the position of the three calibration-plate-mounted reflectors, which allows for the

computation of the relative position of the colored circles in the CCS w.r.t. the platform-mounted reflector in the RCS. In short, we present the following contributions:

- A customized calibration plate that can be used for camera as well as laser tracker measurements in our system setup
- A calibration procedure to establish the relative orientation between the CCS and RCS using camera and laser tracker.

2. Related Work

This section provides an overview of mobile robot systems in the context of industrial environments, which includes production and logistics.

Ground operating mobile robots. Ground operating mobile robots can be categorized into two categories: Automated Guided Vehicles (AGVs) and Autonomous Mobile Robots (AMRs). Keith and La (2024) identify the ability of decision making of AMRs as the main difference between both systems. Oyekanlu et al. (2020) on the other hand, use the term AMR to characterize various types of robot systems, e.g., an AGV can also be an AMR, if it meets certain autonomy criteria. They also note that both terms in literature are often used interchangeably. Zhao and Chidambareswaran (2023) identify four key differences, which apply to AMRs: Independent movement (“Go Anywhere”), diversified applications, high adaptation capabilities (“Zero disruption to production”), and cost effectiveness. To navigate through an environment, landmark-based approaches with robot-mounted cameras have been a long-studied approach, besides lidar and laser triangulation methods (Hu and Gu, 2000; Shneier and Bostelman, 2015). Other than landmarks, robot position can be obtained from known and detected objects based on sensor data (Ben-Ari and Mondada, 2018). Another method for AGV routing is realized through ground-fixed magnetic tape, inductive wire (Shneier and Bostelman, 2015; Zhao and Chidambareswaran, 2023) or laser projection (Tsuruta et al., 2019). For both AMRs and AGVs, SLAM-based approaches are widely used, if no information like CAD models about the environment is provided (Harapanahalli et al., 2019; Wang and Zhang, 2024). If key objects in the environment are known, e.g. through ground truth images, a (visual) SLAM algorithm can be used for independent navigation, if an object detection algorithm is provided (Asadi et al., 2018). The key difference is that AMRs navigate independently, while AGVs strictly follow predefined paths (Zhang et al., 2023; Zhao and Chidambareswaran, 2023).

Optical robot calibration. In this section, we only include calibration methods that relate camera coordination systems to robot coordination systems. Calibration of camera intrinsics (Zhang, 2000) as well as kinematic calibration without optical sensors (Li et al., 2021) are excluded.

Hand-eye calibration describes the determination of the camera pose relative to the robot (Steger et al., 2018). Initially, early hand-eye calibration methods from Lenz and Tsai (1988) and Tsai and Lenz (1989) introduced the terminology of eye-on-hand configuration, whereby the camera is mounted on the last joint of a robot arm with a calibration body or plate in the robot workspace. Those and following methods (Chou and Kamel, 1988; Park and Martin, 1994) first determine rotation, then translation. Simultaneously determining rotation and translation was achieved by follow-up works (Daniilidis and Bayro-Corrochano, 1996; Daniilidis, 1999; Strobl and Hirzinger, 2006),

mainly using dual quaternions to avoid non-linear optimization, with a special application for SCARA-Robots (ISO, 1994, 1999) by Ulrich and Steger (2016). Ulrich and Hillemann (2021, 2024) approach the challenge of uncertainty between the precision of the robot and the absolute accuracy from a geodetic point of view. Ulrich et al. (2024) simultaneously calibrate robot kinematics, the hand-eye transformation, and the intrinsic camera parameters with a robot-mounted camera.

Laser trackers are a common optical measurement system used for kinematic robot calibration (Abderrahim et al., 2006; Chen et al., 2014; Li et al., 2016; Liu et al., 2018), especially for high-precision determination of the position of a robot end-effector. Li et al. (2021) lay out the limitations of such methods, whereby the main disadvantage is that the robot can create self-occlusion w.r.t. the stationary laser tracker. Because a laser tracker is used for kinematic calibration only, Ulrich et al. (2024) point out that a camera-based calibration of the kinematics can be a cost-effective and easy alternative to the calibration using a laser tracker, if a camera is already integrated into the system configuration.

Floor marking and detection. To automatically mark stand positions for exhibitions and trade fairs, Jensfelt et al. (2006) describe an AGV that marks a predefined set of positions on the ground in conjunction with a CAD model of a large facility like an event hall. The average absolute positional accuracy is 28 mm with a standard deviation of 18 mm. Utilized for indoor construction sites but closely related to the objective of the Rita system, Tsuruta et al. (2019) introduced a mobile robot system for floor marking, that follows a laser-projected line on the ground. The robot itself contains cameras to detect the projected lines. Regarding accuracy, the authors state the average deviation (w.r.t. x- and y-direction) with 2.3 mm, and the standard deviation with 1.4 mm. Iqbal et al. (2023) present a system with an accuracy of 10 to 15 mm for a line drawing task. There exists a wide range of research for mobile robot positioning based on fiducial markers that are attached to the wall or ceiling (Mondéjar-Guerra et al., 2018; Romero-Ramirez et al., 2018; Fiala, 2009), or especially ArUco markers (Zheng et al., 2018; Filus et al., 2022). Gwak et al. (2021) propose two special QR-code-like markers, namely hierarchical and nested markers, for horizontally moving mobile robots (e.g., AGVs) as well as robots with the ability to move vertically (e.g., UAVs), respectively. The problem of robot positioning is closely related to camera pose estimation, which is a fundamental photogrammetric problem and typically solved by spatial resection and bundle adjustment while exploiting the epipolar constraint for stereo pose initialization within a multi-view setup. These methods are used in modern Structure-from-Motion (SfM) (Schoenberger and Frahm, 2016) or visual SLAM (Mur-Artal et al., 2015) algorithms, however, with the constraint of identifying matching keypoints in corresponding images or keyframes. Works by Nguyen et al. (2017) and Zhang et al. (2021) focus on the health-related task of visual-impairment, using a mobile robot as an assistive system with integrated path planning. Especially cameras and active sensors are utilized, while Odometry and SLAM are used for positioning and mapping. Line and lane detection are further tasks for robot systems with onboard optical sensors, especially for the task of autonomous driving (Gajjar et al., 2023) and for AGVs in industry (Liu et al., 2020; Zhang, 2023). The Mark.One robot as a commercial product is a robot system for floor mark detection, which achieves a positioning accuracy of 1 mm (SOLID3D, 2025) using a built-in ground-facing camera. Additionally, a stationary laser tracker is in-

cluded in the system configuration.

3. Methodology

In this section, the hardware-induced conditions are laid out with the design of a customized calibration plate as one major contribution. Method concerning assumptions w.r.t. the hardware setup are introduced at first occurrence.

All *coordinate systems* (CS) are assumed to be Euclidean and orthonormal. Cartesian coordinates are used. A point ${}^A P_i$ with index i w.r.t. CS A is a 3-tuple with homogeneous coordinate representation

$${}^A \bar{P}_i = \begin{pmatrix} {}^A P_i \\ 1 \end{pmatrix}. \quad (1)$$

In the following, a homogeneous transformation from CS A to B , denoted by ${}^B H_A$, is expected to be a 4×4 homogeneous matrix representing a rigid transformation, i.e. ${}^B H_A \in SE(3)$. The analogous notation for rotation matrices is ${}^B R_A \in SO(3)$, while ${}^B \mathbf{v}$ is a 3-tuple vector \mathbf{v} w.r.t. B using a small letter without right hand side index.

3.1 System Setup

A multitude of hardware components provide internal canonical coordinate frames. In the following, a precise notation of the used coordinate frames will be emphasized.

Absolute System (ACS, abs) We utilize laser-tracker measurements ${}^{abs} P$ as ground truth. Local laser-tracker coordinates are transformed into a global coordinate frame, denoting the ACS.

Reflector (smr) We use spherically mounted retro-reflectors (smr) defined by their center point ${}^{abs} P_{smr}$ and radius. These are provided as a dedicated laser-tracker measurement target by the manufacturer and mounted into a reflector nest. While simple ring-shaped steel reflector nests do not provide ideal conditions for μm precise measurements, they are sufficient for sub-mm precise measurements and offer a favorable shape for automatic detection in images.

Robot (RCS, rob) As a reference system, the differential-drive robot Rita (Naab, 2023; Naab et al., 2025) is used. Though the left and right drive wheels as well as the caster wheel are moving parts, the respective wheel contact points with the ground are modeled constant in the robot frame:

$${}^{rob} P_w = \text{const}, \quad (2)$$

$$w \in \{w_{\text{left}}, w_{\text{right}}, w_{\text{passive}}\}. \quad (3)$$

Furthermore, the robot possesses an smr which is always turned into the direction of the laser-tracker. The movement of the smr in the robot chassis is expected to be in sub-mm range, so it can be modeled as the RCS origin:

$${}^{abs} P_{rob} = {}^{abs} P_{smr}, \quad (4)$$

$${}^{rob} P_{smr} = (0 \ 0 \ 0)^\top. \quad (5)$$

The three wheel contact points ${}^{abs} P_w$ do also define an ideal support plane underneath the robot. Based on the support plane normal ${}^{abs} \mathbf{n}$ (upside), the heading direction ${}^{abs} \mathbf{v}$ which yields

${}^{abs} \mathbf{v}_\perp$ as the normalized orthogonal projection of ${}^{abs} \mathbf{v}$ to a normal of ${}^{abs} \mathbf{n}$ and ${}^{abs} \mathbf{c} = {}^{abs} \mathbf{n} \times {}^{abs} \mathbf{v}_\perp$ completing a right-handed orthonormal basis, the robot orientation

$${}^{abs} R_{rob} = [{}^{abs} \mathbf{v}_\perp \quad {}^{abs} \mathbf{c} \quad {}^{abs} \mathbf{n}] \in SO(3) \quad (6)$$

is defined in the ACS. Combining Eqs. (4) and (6) yields:

$${}^{abs} H_{rob} = \begin{bmatrix} {}^{abs} R_{rob} & {}^{abs} P_{rob} \\ 0 & 1 \end{bmatrix}. \quad (7)$$

Camera (CCS, cam) A ground-facing camera is rigidly attached inside the robot. This camera observes a ground area spanning over a few cm^2 on the floor underneath the robot. At this point, the associated camera model is assumed to be calibrated in advance. A ruggedized lens has been selected that preserves this calibration over time and is not affected by shocks or vibrations. This leads to the assumption that the CCS is fixed in the RCS:

$${}^{rob} H_{cam} = \text{const}. \quad (8)$$

Referencing Plate (PCS, ref) A referencing plate (Fig. 5) was designed to combine the two measurement modalities of laser-tracker 3D metrology and camera-based 2D imaging. On the one hand side, it provides reflector nests to obtain the pose in the ACS. On the other hand side, it integrates a camera calibration target on the surface, which can be measured by the camera when the robot moves over the plate. For this, we use a calibration target (MVTec Software GmbH, 2025) which supports determining a unique pose by coded markers. The corresponding rigid transformation is denoted by ${}^{cam} H_{ref}$. The material ensures that the surface conforms to a plane within sub-millimeter tolerances and remains undeformed under robot load. Reflector nests ring surfaces are expected to be even or at least parallel to the surface. The surface must be on the xy-plane of the PCS, which is given by the integrated calibration target. This will also be the reference system for the referencing plate.

3.2 Referencing

The core idea of our referencing method is to retrieve

- the camera pose relative to the referencing plate,
- the plate pose in the abs system and
- the robot pose in the abs system,

when the robot is placed on the referencing plate such that the integrated calibration target is visible in the camera image. The transformations are visualized in Fig. 2.

Scene (SCS, scn) The scene describes a concept in the context of image rectification. Polynomial camera model parameters and ${}^{cam} H_{ref}$ are sufficient to project points from the image plane into the PCS-xy-plane. The SCS is chosen such that the projection of the entire image of the camera fits into the positive xy-quadrant and x- and y-axis are aligned to image row and column (z-axis pointing upwards now, contrarily to PCS). The calculation of the rectification map

$$\text{map}_{image}^{scn-xy} : \mathbb{R}^2 \mapsto \mathbb{R}^2, \quad (9)$$

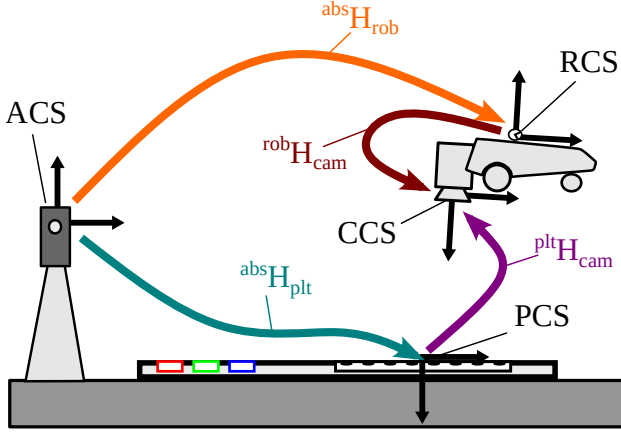


Figure 2. Retrieval of the orientation of the camera inside the robot frame. The plate-absolute-transformation $^{abs}H_{plt}$ and the plate-camera-transformation $^{plt}H_{cam}$, as well as the robot-absolute-transformation $^{abs}H_{rob}$ on the other side, are combined to robot-camera-transformation $^{rob}H_{cam}$ (figure adapted from Ulrich and Hillemann (2024)).

that maps image points directly into positive SCS-xy-plane yields $^{scn}H_{cam}$. In this contribution, image-based measurements are directly represented in the SCS. The conceptual advantage is the following: While the PCS is bound to the referencing plate, the SCS is bound to the CCS and therefore the RCS, even when the robot moves. It directly denotes the location of the rectified image on the floor, assuming planarity in between the wheel contact points $^{abs}P_w$.

Referencing plate measurement As a preparation, some points of the referencing plate have to be measured once. For this purpose, a stereo vision setup (Fig. 3) is used to determine 3D points. First, the actual positions of the calibration target circles have to be determined. Additionally, there are three reflector nests integrated into the plate, called $n_r, n_g,$ and n_b (using color codes in practice). In the stereo vision setup, the ring-shaped surface of the steel reflector nests is matched and their center $^{ref}P_{nst,i}, i \in \{n_r, n_g, n_b\}$ is determined relative to the PCS. Assuming the plane that is defined by the reflector nests is parallel to the plate, it is just a z-shift by a known offset δ_{nst} to retrieve the effective smr position, when mounted:

$$^{ref}P_{smr,i} = ^{ref}P_{nst,i} - \begin{pmatrix} 0 \\ 0 \\ \delta_{smr,nst} \end{pmatrix}. \quad (10)$$

When δ_{nst} is determined as a positive distance, it must be subtracted, because the PCS z-axis mounts into the referencing plate.

Plate pose estimation For each integrated reflector nest in the referencing plate, i.e., $i \in \{n_r, n_g, n_b\}$, the laser-tracker measures the position $^{abs}P_i := ^{abs}P_{smr,i}$ of a mounted smr in ACS. The same position is known in the PCS: $^{ref}P_i := ^{ref}P_{smr,i}$. Using the transformation

$$^{scn}H_{ref} = ^{scn}H_{cam} ^{cam}H_{ref}, \quad (11)$$

it can be transformed into the SCS by

$$^{scn}\bar{P}_i = ^{scn}H_{ref} ^{ref}\bar{P}_i. \quad (12)$$

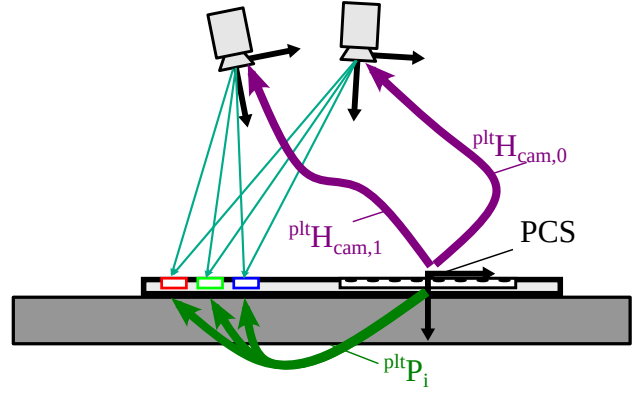


Figure 3. Stereo measurement of the reflector nest positions in the referencing plate frame. The plate-camera-transformations $^{plt}H_{cam,0}$ and $^{plt}H_{cam,1}$ are used to calculate the reflector nest positions $^{plt}P_i$ by triangulation (turquoise arrows) (figure adapted from Ulrich and Hillemann (2024)).

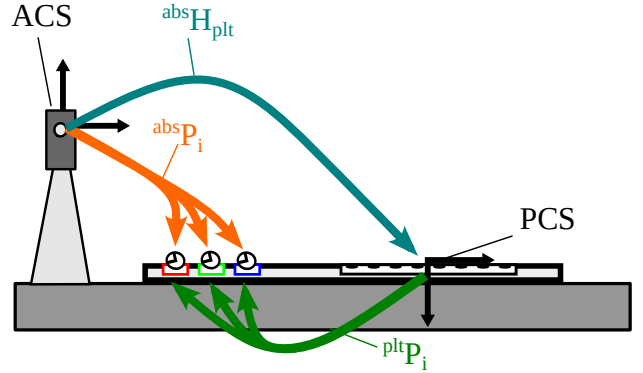


Figure 4. Retrieval of the absolute orientation of the referencing plate. Absolute laser-tracker-measurements $^{abs}P_i$ are matched to the reflector nest positions w.r.t. the referencing plate, yielding the absolute-plate-transformation $^{abs}H_{plt}$ (figure adapted from Ulrich and Hillemann (2024)).

Matching these points together yields the transformation from SCS to the ACS:

$$^{abs}H_{scn} = \arg \min_{^{abs}\tilde{H}_{scn}} \sum_{i \in \{n_r, n_g, n_b\}} \|^{abs}\bar{P}_i - ^{abs}\tilde{H}_{scn} ^{scn}\bar{P}_i\|^2 \quad (13)$$

Robot pose estimation If the robot is placed on the referencing plate arbitrarily in the world, the measured smr position yields $^{abs}P_{rob,0}$ directly, but the basis vectors of the robot orientation $^{abs}R_{rob}$ as stated above have to be retrieved. The upward directed normal of the referencing plate surface is

$$^{abs}\tilde{\mathbf{n}} = \begin{pmatrix} ^{abs}P_b - ^{abs}P_r \end{pmatrix} \times \begin{pmatrix} ^{abs}P_g - ^{abs}P_r \end{pmatrix}, \quad (14)$$

$$^{abs}\mathbf{n} = \frac{^{abs}\tilde{\mathbf{n}}}{\|^{abs}\tilde{\mathbf{n}}\|}. \quad (15)$$

The normal depends on the actual configuration of $n_r, n_g,$ and n_b . To retrieve the robots heading direction, it must move to a second position. The calculated pose relates to $^{abs}P_{rob,0}$, which also relates to the image, which yields $^{cam}H_{ref}$. The second robot position $^{abs}P_{rob,1}$ is only used to determine the movement

vector

$${}^{abs}\tilde{\mathbf{v}} = {}^{abs}P_{rob,1} - {}^{abs}P_{rob,0}, \quad (16)$$

$${}^{abs}\tilde{\mathbf{v}}_{\perp} = {}^{abs}\tilde{\mathbf{v}} - \left({}^{abs}\tilde{\mathbf{v}} \cdot {}^{abs}\mathbf{n} \right) {}^{abs}\mathbf{n}, \quad (17)$$

$${}^{abs}\mathbf{v}_{\perp} = \frac{{}^{abs}\tilde{\mathbf{v}}_{\perp}}{\|{}^{abs}\tilde{\mathbf{v}}_{\perp}\|}. \quad (18)$$

The orthonormal basis (see Eq. (6)) yields the robot orientation

$${}^{abs}R_{rob} = [\mathbf{v}_{\perp} \quad \mathbf{c} \quad \mathbf{n}] = [{}^{abs}\mathbf{v}_{\perp} \quad {}^{abs}\mathbf{c} \quad {}^{abs}\mathbf{n}] \quad (19)$$

and consequently the complete transformation (see Eq. (7)):

$${}^{abs}H_{rob} = \begin{bmatrix} {}^{abs}R_{rob} & {}^{abs}P_{rob,0} \\ 0 & 1 \end{bmatrix}, \quad (20)$$

$${}^{rob}H_{abs} \stackrel{SE(3)}{=} {}^{abs}H_{rob}^{-1} \quad (21)$$

Finally, the composite transformation from SCS to RCS is

$${}^{rob}H_{scn} = {}^{rob}H_{abs} {}^{abs}H_{scn} \quad (22)$$

and the more intuitive transformation from CCS to RCS is

$${}^{rob}H_{cam} = {}^{rob}H_{scn} {}^{scn}H_{cam}. \quad (23)$$

4. Mark measurement and experimental setup

The verification of our method in practice is inspired by our actual use case. The idea is to measure one point on the floor from different perspectives and assume the results to be equal.

In the experiments we use the mobile robot Rita (Fig. 1) equipped with a *LUCID Vision Labs Phoenix PHX122S, 12.2 MP, Sony IMX226* with an *Edmund Optics CR-Series 3.5 mm* lens mounted. The *Leica Absolute Tracker AT901* is used for robot positioning (not covered in this work) as well as the measurements of the proposed method and experiments.

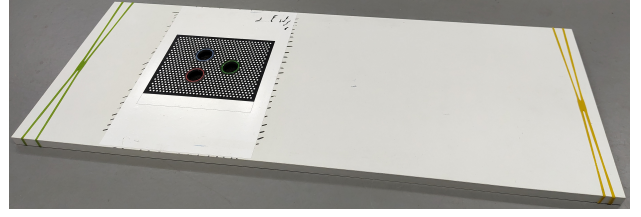
Referencing A set of camera intrinsic model parameters is expected to be present as stated in Section 3.1. The referencing method is then executed using the laser-tracker and the mobile robot. To minimize side effects from the robot or the environment, the instrument reversal technique is applied analogously to Evans et al. (1996).

Point measurement The point on the floor is marked with a specific shape (mrk). In the image, the center point $(row_{mrk}, column_{mrk})^T$ of this mark is measured subpixel-precisely by using shape-based matching (Steger et al., 2018). Using the rectification map (Eq. (9)), it can directly be mapped into the SCS and transformed into the RCS:

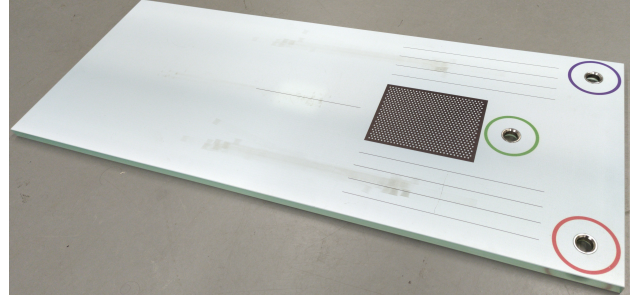
$${}^{rob}\bar{P}_{mrk} = {}^{rob}H_{scn} \left(\text{map}_{image}^{scn-xy} \begin{pmatrix} row_{mrk} \\ column_{mrk} \\ 0 \\ 1 \end{pmatrix} \right). \quad (24)$$

When the robot pose ${}^{abs}H_{rob}$ is known while taking the measurement image, the abs point is obtained by

$${}^{abs}\bar{P}_{mrk} = {}^{abs}H_{rob} {}^{rob}\bar{P}_{mrk}. \quad (25)$$



(a) In-house-designed wooden referencing plate demonstrator which is not sufficiently flat and can be deformed by the mobile robot weight. Green and yellow rubber band is applied against slipping.



(b) Bespoke referencing plate which is made of 19mm thick glass providing a flat and stable surface.

Figure 5. Referencing plates used in experiments. While they are arbitrarily posed on the ground, a mobile robot Rita can be placed on them. The colored circles mark flush-mounted reflector nests. The dark texture represents the HALCON calibration target with circular marks. The rest of the white area provides space to move the robot for a few decimeters.

Floor inclination As long as no high quality IMU is integrated, the measurement result may be shifted by some floor inclination. Since this shift is related to the floor which is fixed in the ACS, it is independent of the robot pose. Therefore this effect will not be covered by the proposed experiment.

Experiment setup While z , roll, and pitch passively depend on the environment, the x and y position of the robot are actively varied, so that row_{mrk} and $column_{mrk}$ appear at different locations while remaining visible in the image. Employing eight equidistant yaw angles enables a thorough assessment and visualization of calibration errors.

Referencing plate design Fig. 5 shows the referencing plates used in the experiments. The assumptions about this plate forced us to evolve the design over time. In an early stage, there was an in-house-designed wooden referencing plate demonstrator available, see Fig. 5(a). Large calibration errors could be related to the material and planarity of the calibration target, where the reflector nests were set flush. In a further step, these error sources were addressed by designing a glass plate that easily supports the robot weight, see Fig. 5(b). The reflector nests are placed outside the calibration target so this is not deformed.

5. Results

Wooden demonstrator referencing plate Using the wooden referencing plate, which especially breaks assumptions about the planarity, our experiments show a major calibration error. Repeated measurements of one printed mark on the floor show a systematic error depending on the robot heading. The robot approached the mark from eight different directions, an image

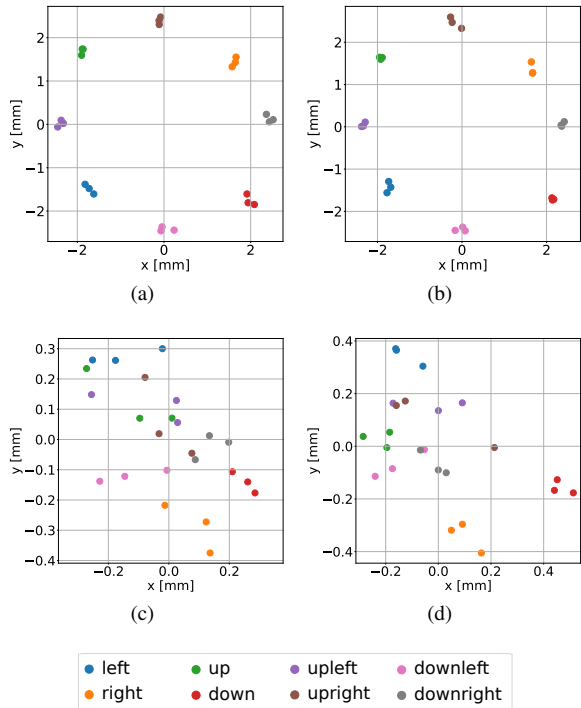


Figure 6. Results of repeated absolute measurements of marks on the floor in an experiment. Each plot is normalized to the overall mean position, see Table 1. (a) and (c) denote the same point as Table 1 does. (b) and (d) denote another mark on the floor. (a) and (b) are based on the in-house-designed wooden referencing plate. (c) and (d) are based on the bespoke glass referencing plate

was taken, and the position of the mark was measured and calculated consequently. The measurement results are clustered in eight regions, depending on the approach direction as shown in Figs. 6(a) and 6(b) for two different printed marks on the floor.

Bespoke glass referencing plate Figs. 6(c) and 6(d) show the same experiment for the glass plate. The same clusters are also distinguishable, but Tab. 1 shows the diameter, calculated from the radius $d_i = 2r_i$ with i varying over the eight directions, of the enclosing circle of all measurements $d_{All} = 0.747$ mm is significantly below a millimeter, while the cluster diameters themselves range from $d_{Down} = 0.103$ mm to $d_{Up} = 0.326$ mm.

6. Discussion

Dominant error For the in-house-designed referencing plate, Figures 6(a) and 6(b) show the expected disposition of the clusters for a wrong transformation between camera and robot. The measurements are equally shifted away from each direction. If a systematic error in the transformation between camera and robot ${}^{rob}H_{cam}$, see Eq. (23), is dominant, this circular arrangement of clusters is expected. In this case, there are some assumptions missed, which can cause an error in ${}^{rob}H_{cam}$. Since the glass plate successfully addresses these assertions as stated above, these clusters do not show this systematic error. The calibration has reached a sub-mm level and does not remain the dominant error source in the proposed experiment.

Absolute Measurement The most obvious error source is about the missing robot pitch and roll during the test measurements.

Taking the normal vector of the referencing plate to determine the robot's pitch and roll (see Eq. (14)) there is no need for an intrinsic measurement of the robot rotation during the referencing method. The proposed experiment to verify the referencing method is comparing altered, repeated measurement results against each other, where no absolute ground truth is involved. However, when a mark on the floor is measured, the robot's roll and pitch have also to be taken into account to obtain the real absolute coordinate of this mark. Unfortunately, no IMU is yet available which delivers high quality rotation information. Applying an IMU will therefore not change the referencing method itself, but the test, in which the absolute position of a mark is checked in the ACS, will be affected. Then the method can be verified by comparing an absolute measurement against an absolute ground truth.

7. Conclusion

When a mobile robot possesses a ground-facing camera whose orientation must be known in the robot frame to make high precision measurements, even state-of-the-art methods like hand-eye calibration show major disadvantages. In this work, we proposed an alternative solution and showed that the proposed methodology is feasible. A special referencing plate was engineered to connect the optically defined PCS via three reflector nests to the world-defined ACS. Using this referencing plate, the absolute camera pose as well as the absolute robot pose can be retrieved. Combining these poses yields the camera pose w.r.t. the robot. The results have shown errors in sub-mm range which will be further improved in future by involving an IMU.

Acknowledgments

This Project is supported by the Federal Ministry for Economic Affairs and Climate Action (BMWK) on the basis of a decision by the German Bundestag.

References

- Abderrahim, M., Khamis, A., Garrido, S., Moreno, L., 2006. Accuracy and calibration issues of industrial manipulators. *Industrial Robotics: Programming, Simulation and Application*, IntechOpen.
- Asadi, K., Ramshankar, H., Pullagurra, H., Bhandare, A., Shanbhag, S., Mehta, P., Kundu, S., Han, K., Lobaton, E., Wu, T., 2018. Vision-based integrated mobile robotic system for real-time applications in construction. *Automation in Construction*, 96.
- Ben-Ari, M., Mondada, F., 2018. *Elements of Robotics*. Springer, Cham.
- Chen, G., Wang, H., Lin, Z., 2014. Determination of the identifiable parameters in robot calibration based on the POE formula. *IEEE Transactions on Robotics*, 30(5).
- Chou, J. C. K., Kamel, M., 1988. Quaternions approach to solve the kinematic equation of rotation of a sensor-mounted robotic manipulator. *IEEE International Conference on Robotics and Automation (ICRA)*.
- Daniilidis, K., 1999. Hand-eye calibration using dual quaternions. *The International Journal of Robotics Research*, 18.

Direction	Mean Position [mm]		Distance Metrics [mm]			Approach Angle Range [°]
	X	Y	Max from Mean	Mean from Mean	Cluster Radius	
left	130825.822	8525.577	0.131	0.098	0.117	[89.48, 90.66]
right	130826.054	8525.014	0.119	0.094	0.109	[-90.40, -89.96]
up	130825.853	8525.427	0.188	0.140	0.163	[0.12, 0.36]
down	130826.224	8525.161	0.054	0.042	0.052	[179.53, 179.68]
upleft	130825.905	8525.413	0.192	0.139	0.150	[45.00, 45.06]
upright	130825.960	8525.362	0.160	0.124	0.148	[-45.11, -44.87]
downleft	130825.845	8525.182	0.122	0.093	0.113	[135.27, 135.43]
downright	130826.112	8525.281	0.070	0.056	0.063	[-135.27, -134.47]
All	130825.972	8525.302	0.399	0.239	0.374	

Mean L2-distance between cluster means: 0.215 mm

Table 1. Quantitative results of repeated absolute measurements of marks on the floor in an experiment. Individual (non-averaged) measured positions of this experiment are plotted in 6(c). *Mean position* is the mean of the measured absolute coordinates of the respective cluster. *Max. and mean from mean* denote the (max. and mean, respectively) distance to this *mean position*. *Cluster diameter* is the max. distance between two points in the cluster. In the last row, those metrics are calculated for *all* directions together.

- Daniilidis, K., Bayro-Corrochano, E., 1996. The dual quaternion approach to hand-eye calibration. *Proceedings of the 13th International Conference on Pattern Recognition*, 1.
- Evans, C. J., Hocken, R. J., Estler, W. T., 1996. Self-Calibration: Reversal, Redundancy, Error Separation, and 'Absolute Testing'. *CIRP Annals*, 45(2), 617-634.
- Fiala, M., 2009. Designing Highly Reliable Fiducial Markers. *IEEE Transactions on Pattern Analysis and Machine Intelligence*, 32.
- Filus, K., Sobczak, Ł., Domańska, J., Domański, A., Cupek, R., 2022. Real-time testing of vision-based systems for agvs with aruco markers. *IEEE International Conference on Big Data*.
- Gajjar, H., Sanyal, S., Shah, M., 2023. A comprehensive study on lane detecting autonomous car using computer vision. *Expert Systems with Applications*, 233.
- Gasparetto, A., Scalera, L., 2019. A Brief History of Industrial Robotics in the 20th Century. *Advances in Historical Studies*, 8.
- Gwak, D. G., Yang, K. M., Park, M. R., Hahm, J., Koo, J., Lee, J., Seo, K. H., 2021. Marker-Based Method for Recognition of Camera Position for Mobile Robots. *Sensors*, 21(4).
- Harapanahalli, S., O' Mahony, N., Hernandez, G. V., Campbell, S., Riordan, D., Walsh, J., 2019. Autonomous Navigation of mobile robots in factory environment. *Procedia Manufacturing*, 38.
- Hu, H., Gu, D., 2000. Landmark-based navigation of industrial mobile robots. *Industrial Robot*, 27(6).
- Iqbal, F., Ahmed, S., Amin, F., Qayyum, S., Ullah, F., 2023. Integrating BIM-IoT and Autonomous Mobile Robots for Construction Site Layout Printing. *Buildings*, 13(9).
- ISO, 1994. Manipulating industrial robots – Vocabulary. Standard, International Organization for Standardization, Geneva, CH.
- ISO, 1999. Manipulating industrial robots – Coordinate systems and motion nomenclatures. Standard, International Organization for Standardization, Geneva, CH.
- Jensfelt, P., Gullstrand, G., Förel, E., 2006. A mobile robot system for automatic floor marking. *Journal of Field Robotics*, 23.
- Keith, R., La, H. M., 2024. Review of Autonomous Mobile Robots for the Warehouse Environment. *arXiv preprint arXiv:2406.08333*. <https://arxiv.org/abs/2406.08333>.
- Lenz, R. K., Tsai, R. Y., 1988. Calibrating a cartesian robot with eye-on-hand configuration independent of eye-to-hand relationship. *Proceedings of the CVPR '88: The Computer Society Conference on Computer Vision and Pattern Recognition*.
- Li, C., Wu, Y., Löwe, H., Li, Z., 2016. POE-based robot kinematic calibration using axis configuration space and the ad-joint error model. *IEEE Transactions on Robotics*, 32(5).
- Li, Z., Li, S., Luo, X., 2021. An Overview of Calibration Technology of Industrial Robots. *IEEE/CAA Journal of Automatica Sinica*, 8(1).
- Liu, H., Zhu, W., Dong, H., Ke, Y., 2018. An improved kinematic model for serial robot calibration based on local POE formula using position measurement. *Industrial Robot*, 45(5).
- Liu, S., Xiong, M., Zhong, W., Xiong, H., 2020. Towards industrial scenario lane detection: Vision-based agv navigation methods. *IEEE International Conference on Mechatronics and Automation (ICMA)*.
- Mondéjar-Guerra, V., Garrido-Jurado, S., Muñoz-Salinas, R., Marín-Jiménez, M. J., Medina-Carnicer, R., 2018. Robust identification of fiducial markers in challenging conditions. *Expert Systems with Applications*, 93.
- Mur-Artal, R., Montiel, J. M. M., Tardós, J. D., 2015. ORB-SLAM: A Versatile and Accurate Monocular SLAM System. *IEEE Transactions on Robotics*, 31(5), 1147–1163.
- MVTec Software GmbH, 2025. MVTec HALCON 25.11. <https://www.mvtec.com/products/halcon>. Software, version 25.11. Accessed November 17, 2025.
- Naab, C., 2023. A mobile robot for monitoring floor flatness in real-time. *Journal of Applied Geodesy*, 17(2), 109–117. <https://doi.org/10.1515/jag-2022-0046>.
- Naab, C., Runge, P., Ambs, F., Rudolph, J. A., 2025. Rita development. <https://www.gik.kit.edu/>. Web presentation, Accessed April 8, 2025.
- Nguyen, Q. H., Vu, H., Tran, T. H., 2017. Developing a way-finding system on mobile robot assisting visually impaired people in an indoor environment. *Multimedia Tools and Applications*, 76.

- Oyekanlu, E. A., Smith, A. C., Thomas, W. P., Mulroy, G., Hitesh, D., Ramsey, M., Kuhn, D. J., McGhinnis, J. D., Buonavita, S. C., Looper, N. A., Ng, M., Ng'oma, A., Liu, W., McBride, P. G., Shultz, M. G., Cerasi, C., Sun, D., 2020. A Review of Recent Advances in Automated Guided Vehicle Technologies: Integration Challenges and Research Areas for 5G-Based Smart Manufacturing Applications. *IEEE Access*, 8.
- Park, F. C., Martin, B., 1994. Robot Sensor Calibration: Solving $AX = XB$ on the Euclidean Group. *IEEE Transactions on Robotics and Automation*, 10.
- Perez-Grau, F. J., Martinez-de Dios, J. R., Paneque, J. L., Acevedo, J. J., Torres-González, A., Viguria, A., Astorga, J. R., Ollero, A., 2021. Introducing autonomous aerial robots in industrial manufacturing. *Journal of Manufacturing Systems*, 60.
- Romero-Ramirez, F. J., Muñoz-Salinas, R., Medina-Carnicer, R., 2018. Speeded up detection of squared fiducial markers. *Image and Vision Computing*, 76.
- Schoenberger, J. L., Frahm, J.-M., 2016. Structure-from-motion revisited. *IEEE Conference on Computer Vision and Pattern Recognition (CVPR)*.
- Shneier, M., Bostelman, R., 2015. Literature review of mobile robots for manufacturing. National Institute of Standards and Technology (NIST) Report, <https://tsapps.nist.gov/publication/>. Report, Accessed April 8, 2025.
- SOLID3D, 2025. Mark.one product description. <https://www.solid-3d.com/product/>. Product, Accessed April 8, 2025.
- Steger, C., Ulrich, M., Wiedemann, C., 2018. *Machine Vision Algorithms and Applications*. Wiley-VCH.
- Strobl, K. H., Hirzinger, G., 2006. Optimal hand-eye calibration. *Proceedings of the IEEE/RSJ International Conference on Intelligent Robots and Systems (IROS 2006)*.
- Tehrani, B. M., Buhamdan, S., Alwisy, A., 2022. Robotics in assembly-based industrialized construction: a narrative review and a look forward. *International Journal of Intelligent Robotics and Applications*, 7.
- Tsai, R. Y., Lenz, R. K., 1989. A new technique for fully autonomous and efficient 3D robotics hand/eye calibration. *IEEE Transactions on Robotics and Automation*, 5(3).
- Tsuruta, T., Miura, K., Miyaguchi, M., 2019. Mobile robot for marking free access floors at construction sites. *Automation in Construction*, 107.
- Ulrich, M., Hillemann, M., 2021. Generic hand-eye calibration of uncertain robots. *2021 IEEE International Conference on Robotics and Automation (ICRA)*, Xi'an, China.
- Ulrich, M., Hillemann, M., 2024. Uncertainty-Aware Hand-Eye Calibration. *IEEE Transactions on Robotics*, 40.
- Ulrich, M., Steger, C., 2016. Hand-Eye Calibration of SCARA Robots Using Dual Quaternions. *Pattern Recognition and Image Analysis*, 16(1).
- Ulrich, M., Steger, C., Butsch, F., Liebe, M., 2024. Vision-guided robot calibration using photogrammetric methods. *ISPRS Journal of Photogrammetry and Remote Sensing*, 218.
- Wang, S., Zhang, W., 2024. Slam algorithms for autonomous mobile robots. *Emerging Methodologies and Applications in Modelling – Modeling, Identification, and Control for Cyber-Physical Systems Towards Industry 4.0*, Academic Press.
- Zamalloa, I., Kojcev, R., Hernandez, A., Muguruza, I., Usategui, L., Bilbao, A., Mayoral, V., 2017. Dissecting Robotics – Historical Overview and Future Perspectives. *arXiv preprint arXiv:1704.08617*. <https://arxiv.org/abs/1704.08617>.
- Zhang, H., Jin, L., Ye, C., 2021. An RGB-D Camera Based Visual Positioning System for Assistive Navigation by a Robotic Navigation Aid. *IEEE/CAA Journal of Automatica Sinica*, 8(8).
- Zhang, J., Yang, X., Wang, W., Guan, J., Ding, L., Lee, V. C. S., 2023. Automated guided vehicles and autonomous mobile robots for recognition and tracking in civil engineering. *Automation in Construction*, 146.
- Zhang, N., 2023. Navigation and obstacle avoidance technology for warehouse tracking AGVs based on multi-sensor information fusion. *2023 IEEE 2nd International Conference on Electrical Engineering, Big Data and Algorithms (EEBDA)*.
- Zhang, Z., 2000. A flexible new technique for camera calibration. *IEEE Transactions on Pattern Analysis and Machine Intelligence*, 22(11).
- Zhao, X., Chidambareswaran, T., 2023. Autonomous mobile robots in manufacturing operations. *2023 IEEE 19th International Conference on Automation Science and Engineering (CASE)*, Auckland, New Zealand.
- Zheng, J., Bi, S., Cao, B., Yang, D., 2018. Visual localization of inspection robot using extended kalman filter and aruco markers. *IEEE International Conference on Robotics and Biomimetics (ROBIO)*, Kuala Lumpur, Malaysia.